



Article

Developing a Se Quantum Dots@ CoFeO_x Composite Nanomaterial as a Highly Active and Stable Cathode Material for Rechargeable Zinc–Air Batteries

Donghao Zhang ¹ **Yang Wang** ^{1,2}, **Xiaopeng Han** ¹ and **Wenbin Hu** ^{1,3,*}

¹ Tianjin Key Laboratory of Composite and Functional Materials, Key Laboratory of Advanced Ceramics and Machining Technology (Ministry of Education), School of Materials Science and Engineering, Tianjin University, Tianjin 300350, China; xphan@tju.edu.cn (X.H.)

² State Key Laboratory of Marine Resource Utilization in South China Sea, School of Materials Science and Engineering, Hainan University, Haikou 570228, China

³ Joint School of National University of Singapore and Tianjin University, International Campus of Tianjin University, Binhai New City, Fuzhou 350207, China

* Correspondence: wbhu@tju.edu.cn

Abstract: With the urgent demand for clean energy, rechargeable zinc–air batteries (ZABs) are attracting increasing attention. Precious-metal-based electrocatalysts (e.g., commercial Pt/C and IrO₂) are reported to be highly active towards the oxygen reduction reaction (ORR) and oxygen evolution reaction (OER). Nevertheless, the limited catalytic kinetics, along with the scarcity of noble metals, still hinder the practical applications of ZABs. Consequently, it is of great importance to explore efficient bifunctional ORR/OER electrocatalysts with abundant reserves. Although iron oxides are considered to have some of the greatest potential as catalysts among the metal oxides, owing to their excellent redox properties, lower toxicity, simple preparation, and natural abundance, their poor electrical conductivity and high agglomeration still limit their development. In this work, we report a special Se quantum dots@ CoFeO_x (Se-FeO_x-Co) composite material, which exhibits outstanding bifunctional catalytic properties. And the potential gap between ORR and OER is low at 0.87 V. In addition, the ZAB based on Se-FeO_x-Co achieves a satisfactory open-circuit voltage (1.46 V) along with an operation durability over 800 min. This research explores an effective strategy to fabricate iron oxide-based bifunctional catalysts, which contributes to the future design of related materials.



Citation: Zhang, D.; Wang, Y.; Han, X.; Hu, W. Developing a Se Quantum Dots@ CoFeO_x Composite Nanomaterial as a Highly Active and Stable Cathode Material for Rechargeable Zinc–Air Batteries. *Batteries* **2023**, *9*, 561. <https://doi.org/10.3390/batteries9110561>

Academic Editor: Dino Tonti

Received: 6 October 2023

Revised: 25 October 2023

Accepted: 27 October 2023

Published: 17 November 2023



Copyright: © 2023 by the authors. Licensee MDPI, Basel, Switzerland. This article is an open access article distributed under the terms and conditions of the Creative Commons Attribution (CC BY) license (<https://creativecommons.org/licenses/by/4.0/>).

1. Introduction

In recent years, the overuse of fossil resources has brought about increasingly serious energy crises and environmental pollution. To meet global energy demands, it is strongly necessary to explore clean renewable energy. Electrochemical energy storage devices with sufficient energy output, stable performance, and high energy density are drawing increasing attention. Among the various devices, batteries (including metal-ion batteries and metal–air batteries) are regarded as the most promising energy technologies [1,2]. Among the various kinds of batteries, rechargeable zinc–air batteries (ZABs) are receiving great interest owing to many advantages, such as high energy density, environmental friendliness, and the abundance of Zn raw materials [3–5]. A reversible air–cathodic electrochemical reaction ($O_2 + 2H_2O + 4e^- \leftrightarrow 4OH^-$) proceeds in the catalysts' surfaces, while an anodic electrochemical reaction ($Zn + 4OH^- - 2e^- \rightarrow Zn(OH)_4^{2-}$, $Zn(OH)_4^{2-} \leftrightarrow ZnO + H_2O + 2OH^-$) occurs in Zn plates in the alkaline electrolyte. However, one of the main issues is the suitable selection and design of the bifunctional catalysts as the air cathode. The sluggish kinetics of the oxygen reduction reaction (ORR) and oxygen evolution reaction (OER) of catalysts would lead to a large potential gap and low round-trip efficiency. As a result,

the further development of ZABs is hindered [6,7]. According to the reaction mechanism, the theoretical voltage of ZAB is determined to be 1.65 V. However, the actual working voltage is generally lower than 1.2 V, with a much higher charging voltage (>2 V), and the current round-trip energy efficiency is usually less than 60%. Precious metal catalysts (e.g., commercial Pt/C and IrO₂) prove to be highly active catalysts for ORR and OER [8,9]. The limited reserves still preclude the large-scale applications of ZABs [10]. Consequently, rationally exploring bifunctional ORR/OER electrocatalysts with high activity and abundant reserves is necessary.

To date, non-noble transitional metal-based materials (such as Fe, Co, and Mn), especially sulfide, oxide, phosphide, nitride, and selenide, have been reported to be viable candidates to replace noble metal electrocatalysts because of their remarkable catalytic abilities [11]. As previously reported, Zou and co-workers synthesized a novel catalyst with Co sites anchored with a CoP electrocatalyst for oxygen electrocatalysis in ZAB, exhibiting a high power density of 139.8 mW cm⁻² and rechargeability of 132 h [12]. Zhang et al. prepared a N-doped carbon-tentacles-modified metal (Fe or Co) Se nanomaterial through a scalable as well as facile solid-state strategy, which exhibited superior activity and durability thanks to abundant active sites [13]. Xiao et al. designed Co₃O₄ nanoparticles with atomically dispersed FeN₂, and the FeN₂ was determined to be the real catalytic active site in oxygen electrocatalysis [14]. Ren et al. made a rational design for the heterojunction structure of FeS₂/NiS₂, which has a potential gap of 0.92 V when utilized in a liquid ZAB [15]. Among these, Co, Fe, and Ni-based oxide catalysts have been attracting more and more extensive attention because of their high nontoxicity [16–19]. In particular, ABO₃-type perovskites and the AB₂O₄-type spinel oxides have been widely used as bifunctional catalysts in metal-air batteries (A and B are different metal elements) [20–23]. It is worth mentioning that metal oxides can provide abundant oxidized metal sites on the catalyst surface and are easy to tune and affect the electronic structure, thereby improving the electrocatalysis performance [24].

Although Co oxides and Ni oxides have been widely reported as bifunctional catalysts in previous works in the literature, iron oxides have been less studied. Iron oxides, as a kind of well-known metal oxide, have attracted numerous research efforts in the scientific and commercial fields because of their excellent redox properties, lower toxicity, simple preparation, and natural abundance [25]. Unfortunately, iron oxides have an inherently poor electrical conductivity and high agglomeration, which would lead to rapid recession and poor cycling durability [26]. This issue creates poor ORR and OER performance in catalysts, so iron-based oxides are still far below expectation. Hence, various strategies have been put forward to improve the unsatisfactory activity or stability of iron oxides, including exposing active sites, reducing their nanoscale, and so on [27–29]. In recent years, designing composite materials with highly conductive additives has been widely reported to significantly improve their dispersion and catalytic activity [30–32]. For example, Wang et al. reported short carbon nanotubes supporting nickel–iron oxides, where the carbon composite confers a high electrochemical surface area and satisfactory electron transfer ability [31]. Li et al. synthesized heterostructural FeO_x/Fe nanoparticles based on a nitrogen-doped carbon framework, which displayed high ORR activity and good durability due to the high electroconductivity and proper hydrophilicity of the carbon framework [33]. However, it is more desirable if the intrinsic conductivity and stability of iron oxide can be substantially boosted, which may result in a breakthrough in catalytic performance. Quantum dots, as a novel 0D material, are widely considered to be one of the most fascinating materials because of their specific electrical, optical, and chemical properties. Due to the small nanometer scale, quantum dots have some specific quantum tunneling effects and quantum size effects, which are widely used in the field of catalysis, optical, and chemical properties. Owing to their small nanometer scale, QDs have specific quantum tunneling and quantum size effects, which are widely harnessed in the fields of catalysis, optical sensing, and solar-harvesting devices [34,35]. The introduction of QDs

into composites can improve their electrocatalytic properties by enhancing their electrical conductivity and energy conversion efficiency [36,37].

Herein, we report a facile one-pot hydrothermal process for synthesizing Co-doped iron oxide nanosheets loaded with Se QDs. The Co precursor ratio was optimized to enhance the ORR and OER performances. The catalytic activity and stability sharply increased when Co was successfully incorporated into the original Fe_2O_3 lattice. In particular, the special Se QD@Co FeO_x (Se- FeO_x -Co) composite material exhibited remarkable catalytic behavior for the alkaline ORR and OER. In detail, the half-wave potential of ORR was 0.64 V. For OER, it required a reduced overpotential (280 mV) to reach 10 mA cm^{-2} . Moreover, when Se- FeO_x -Co served as an air cathode in a ZAB in a liquid electrolyte, the optimized material showed good catalytic activity and stability for at least 800 min. Our results not only explore an effective strategy to optimize the bifunctional performance of iron oxides but also contribute to the future design of energy-related electrocatalysts.

2. Materials and Methods

2.1. Reagents and Materials

Cobaltous nitrate hexahydrate ($\text{Co}(\text{NO}_3)_2 \cdot 6\text{H}_2\text{O}$, 95%) and ammonium iron (II) sulfate hexahydrate ($\text{NH}_4\text{Fe}(\text{SO}_4)_2 \cdot 6\text{H}_2\text{O}$, 98%) were produced by the Adamas Reagent Co., Ltd., Shanghai, China. Zinc acetate dihydrate ($\text{Zn}(\text{CH}_3\text{COO})_2 \cdot 2\text{H}_2\text{O}$) was obtained from Shanghai Macklin Biochemical Co., Ltd., Shanghai, China. Hydrazine hydrate ($\text{N}_2\text{H}_4 \cdot \text{H}_2\text{O}$, AR, 99%) was purchased from the Yuanli Chemical Technology Co., Ltd., Tianjin, China. 5 wt.% Nafion solution was obtained from Sigma-Aldrich Co., Ltd., St. Shanghai, China. Potassium hydroxide (KOH, 95%) was obtained from Jiangtian Chemical Technology Co., Ltd., Tianjin, China.

2.2. Synthesis of Se- FeO_x -Co Composite Materials

Firstly, 1.4 mmol $\text{Co}(\text{NO}_3)_2 \cdot 6\text{H}_2\text{O}$ and 4.2 mmol $\text{NH}_4\text{Fe}(\text{SO}_4)_2 \cdot 6\text{H}_2\text{O}$ were dissolved in 25 mL of deionized water in a clean beaker. After 30 min magnetic stirring, 0.11 g of NH_4Cl , 0.4 g of NH_4F , 0.31 g of SeO_2 , and 5 mL of hydrazine hydrate were added. Then, the mixing solution was transferred into a 50 mL PTFE-lined stainless autoclave and placed in an oven at 180 °C for 12 h. The as-synthesized precipitation was obtained via a centrifugation process. And the product was washed with DI water three times. Then, the products were dried in an oven at 60 °C for 12 h. According to the different addition amounts of $\text{Co}(\text{NO}_3)_2 \cdot 6\text{H}_2\text{O}$ (0.7 and 1.4 mmol), the products were named Se- FeO_x -Co-1 and Se- FeO_x -Co-2, respectively. In addition, the sample to which no Co precursor was added was named Se- FeO_x .

2.3. Materials' Characterization

X-ray diffraction (XRD) (Cu K α radiation, D8 Advanced, 5 min^{-1}) was used to measure the crystal structural information of the samples. The morphologies and characteristic structures of Se- FeO_x -Co series materials were determined using a JSM-7800F field emission scanning electron microscope (SEM). Before characterization, the dried powder samples were added into absolute ethyl alcohol. After ultrasonic dispersion, the black solution was added dropwise to clean and smooth pieces of Al foil. After drying under room temperature, those pieces of Al foil were transferred to the vacuum box of the SEM device. In addition, the above-mentioned solution was further dropped on a copper mesh that supported an ultra-thin carbon film and then treated using a vacuum oven. The interior structure of the Se- FeO_x -Co series materials was then explored via high-resolution transmission electron microscopy (HRTEM), which was carried out with a JEM-2100F device. The Raman spectra of the samples in the range of 100–1600 cm^{-1} were obtained using a multichannel Raman system (Horiba Jobin Yvon, Kyoto, Japan) with a 532 nm laser. The valence states and chemical information of the samples were measured with an energy-dispersive X-ray photoelectron spectroscope (XPS, Axis Supra, Kratos Analytical Ltd., Manchester, UK).

2.4. Electrochemical Measurements

Homogeneous inks from the ORR and OER tests were obtained by ultrasonically dispersing 7 mg of pre-synthesized sample, 3 mg of black carbon, and 35 μ L of Nafion in 965 μ L of isopropanol for 1 h. Then, the inks were drop-casted on electrodes: a rotating ring-disk electrode (RRDE, with a diameter of 5 mm) for the ORR test and a glassy carbon electrode (with diameter of 5 mm) for the OER test. The catalyst loading was calculated to be 2.8 mg cm^{-2} .

All of the electrochemical performance tests (including linear sweep voltammetry (LSV) curves, cyclic voltammetry (CV), and chronoamperometry (CA)) in this study were performed at room temperature on a CS310X multi-channel electrochemical workstation (Corrtest). For the ORR test, the RRDE electrode modified by a catalyst served as the working electrode. The counter electrode was a carbon rod, and the reference electrode was Hg/HgO. All the ORR measurements were tested in a 0.1 M KOH solution. The reversible hydrogen electrode (E_{RHE}) and the measuring potential (E_{SCE}) can be converted via $E_{\text{RHE}} = E_{\text{Hg/HgO}}^{\theta} + 0.059\text{pH} + E_{\text{SCE}}$. Before each CV and LSV test, pure O_2 was purged into the alkaline electrolyte for more than 1 h in order to make the electrolyte saturated. During the LSV tests, the RRDE measurements of the samples were conducted via changing rotation rates (400, 625, 900, 1225, and 1600 rpm). In addition, electrocatalytic performances were compared at 1600 rpm in the O_2 -saturated electrolyte. During the OER test, the working electrode was a catalyst-modified glassy carbon electrode. The counter electrode was a carbon rod and the reference electrode was Hg/HgO. All the OER measurements were tested in a 1 M KOH solution. The pure N_2 was saturated in the electrolyte for eliminating the effect of oxygen in the OER process.

The electrochemical performance of rechargeable Zn-air batteries was tested in a two-electrode system and was analyzed using a multichannel potential station (LAND CT2001A). Carbon cloths were dipped in dilute HNO_3 solution and deionized water under ultrasonic conditions for 30 min several times, and then washed with deionized water and absolute ethyl alcohol. The above-mentioned ink from the catalysts was dropped uniformly onto a hydrophilic carbon cloth (with an area of $1 \times 1 \text{ cm}^2$). And the loading of catalysts on the cathode was calculated to be 2.8 mg cm^{-2} . Moreover, the polished Zn plate as the anode and 6 M KOH + 0.2 M Zn (CH_3COO)₂ as the liquid electrolyte were constitutive of the rechargeable liquid ZABs. All batteries were tested at a current density of 10 mA cm^{-2} .

3. Results and Discussion

Figure 1a schematically illustrates the preparation of the Se-FeO_x-Co catalysts. Briefly, the SeO₂ precursor decomposed to form Se QDs and O₂ during the one-pot hydrothermal process, and O₂ combined with the Fe³⁺ precursor to form iron oxide. Subsequently, numerous Co²⁺ ions were doped into the crystal lattice of the iron oxide. Figure 1b shows that the XRD pattern of Se-FeO_x had clear peaks corresponding to elemental Se (PDF# 06-0362) and Fe₂O₃ (PDF# 39-1346). With the addition of the Co²⁺ precursor, the relative peaks of crystallographic Fe₂O₃ disappeared, indicating that Co affected the lattice formation of the samples. No heterophase was observed in the Se-FeO_x-Co samples, suggesting the successful incorporation of Co ions into Se-FeO_x [38]. The morphologies of the Se-FeO_x-Co series are shown in Figure 1c,d, Figures S1 and S2. Se-FeO_x shows a typical nanoflower structure. As the Co content increased, the 3D flower structure tended to deform in Se-FeO_x-Co-1. The Se-FeO_x-Co-2 sample exhibited a hierarchical structure consisting of two-dimensional (2D) sheets ~100 nm in length. According to previous reports, the unique 2D sheet structure may significantly improve the exposure of the metal centers and is conducive to wetting the electrolyte [39,40]. In addition, the microscopic structure of the Se-FeO_x-Co-2 sample was further explored using HRTEM. As shown in Figure 1e, Se was observed as QDs with sizes of <2 nm. Notably, Se-FeO_x-Co-2 showed that the (311) plane of crystallographic Fe₂O₃ was coated with an amorphous structure. Compared to Se-FeO_x, the crystallinity of Se-FeO_x-Co-2 was much lower, which indicates that Co was successfully incorporated into the original Fe₂O₃ lattice. The EDS elemental mapping analysis in

Figure 1f demonstrates that the Co, Fe, and O atoms are homogeneously dispersed in Se- $\text{FeO}_x\text{-Co-2}$, whereas the Se atoms in the region are mainly aggregated as well-distributed small particles. The atomic contents of Co, Fe, Se, and O were further measured (Figure 1g) and found to be 13.96%, 38.81%, 2.26%, and 44.97%, respectively. Therefore, the distribution of Fe, Co, and O signals is quite uniform throughout the Se- $\text{FeO}_x\text{-Co-2}$ sample, illustrating the successful doping of Co into the Se- FeO_x matrix. The low content and intensity of Se were due to the small number of Se QDs.

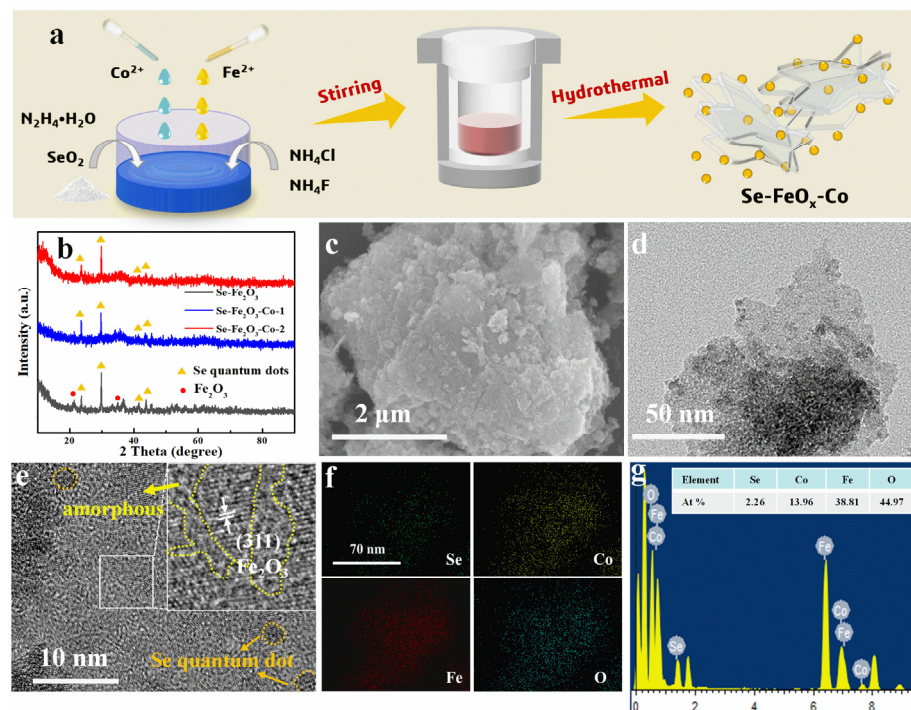


Figure 1. (a) Schematic of the fabrication of Se- $\text{FeO}_x\text{-Co}$. (b) XRD patterns of Se- FeO_x , Se- $\text{FeO}_x\text{-Co-1}$, and Se- $\text{FeO}_x\text{-Co-2}$ samples. (c) SEM, (d) TEM, (e) HRTEM, and (f) EDS mapping images of Se- $\text{FeO}_x\text{-Co-2}$; (g) relative atomic content.

To further explore the structures of the as-synthesized Se- FeO_x and Se- $\text{FeO}_x\text{-Co-2}$ samples, Raman spectra of the two samples were acquired (Figure 2a). On the one hand, the peaks at 216 cm^{-1} belong to the A_{1g} mode of Fe_2O_3 . On the other hand, the peaks at 283 cm^{-1} could be attributed to the $2E_g$ mode of Fe_2O_3 . The peaks at 390 and 594 cm^{-1} in Se- FeO_x are assigned to the E_g modes of Fe_2O_3 . The wide peak at ca. 1300 cm^{-1} is assigned to the second-order scattering of Fe_2O_3 [41,42]. Therefore, the existence of Fe_2O_3 is further suggested for all the samples [43]. In addition, no noticeable peaks are assigned to the Se-O stretching vibration in the Se- FeO_x and Se- $\text{FeO}_x\text{-Co-2}$ samples, indicating the highly stable existence of Se QDs in air with the formation of Se-Se bonds [44]. Notably, the peaks of the two samples slightly differed. Compared with the Se- FeO_x sample, the E_g modes of Fe_2O_3 in the Se- $\text{FeO}_x\text{-Co-2}$ sample slightly changed, and a prominent peak assigned to the E_g mode of O-Co-O bending vibration appeared at 474 cm^{-1} . The structural and valence properties were further investigated using XPS, as shown in Figure 2b–f. The full XPS spectrum in Figure 2b shows typical peaks of Co 2s, Co 2p, Fe 2p, O1s, Fe 3s, Fe 3p, Se 3s, Se 3d, and Se 3p in the Se- $\text{FeO}_x\text{-Co-2}$ sample, indicating the presence of Se, Co, Fe, and O elements. In Figure 2c, the Se 3d spectra of Se- FeO_x and Se- $\text{FeO}_x\text{-Co-2}$ display two characteristic peaks at 54.6 and 55.4 eV belonging to the $\text{Se}^0 3d_{5/2}$ and $\text{Se}^0 3d_{3/2}$ orbits of Se QDs [45,46]. When the Co precursor was added, the characteristic peaks of Se in Se- $\text{FeO}_x\text{-Co-2}$ hardly changed. Thus, we inferred that the doping of Co exerted nearly no influence on the formation of Se QDs. Moreover, the O 1s and Fe 2p spectra show clear differences between the Se- FeO_x and Se- $\text{FeO}_x\text{-Co-2}$ samples. In Figure 2d, the high-resolution

spectrum of elemental oxygen for the catalyst is deconvoluted into peaks at 529.6, 531.2, and 533.2 eV, which correspond to the metal-O bond (Fe-O bond or Co-O bond), oxygen vacancies, and -OH groups (oxygen in the surface-absorbed water molecule) [38,47,48]. In particular, the Se-FeO_x-Co-2 sample had a higher concentration of oxygen vacancies than the Se-FeO_x sample, suggesting that Co ions were successfully incorporated into the FeO_x lattice, thus breaking the bonds between Fe and O atoms. Oxygen vacancies, which are generated by Co doping, are favorable for improving electrical conductivity [49–51]. As shown in Figure 2e, two main peaks at 724.8 and 710.9 eV belong to Fe 2p_{1/2} and Fe 2p_{3/2}, respectively. The fitted curves of Fe 2p_{3/2} are deconvoluted into two peaks at 713.3 and 710.6 eV, which are ascribed to Fe²⁺ and Fe³⁺, respectively [52]. Moreover, the wide peak at 718.6 eV is assigned to the shake-up satellite peak of Fe³⁺ [53,54]. Compared to the Se-FeO_x sample, the Fe 2p spectrum of Se-FeO_x-Co-2 exhibits a positive shift with the successful replacement of Fe by Co, indicating a rich electron state [55]. Furthermore, compared with Se-FeO_x-Co-1, the Co 2p peak of Se-FeO_x-Co-2 also displays a slightly opposite shift (Figure S3), indicating electron acceptance [56]. These shifted binding energies demonstrate a strong electronic interaction between Fe and Co, which promotes the transformation of valence electrons and improves the intrinsic electrocatalytic activity [57]. As shown in Figure 2f, this Co 2p_{1/2} peak can be divided into 787.7, 780.4, and 782.3 eV, corresponding to the satellite peaks of Co³⁺ and Co²⁺, respectively [58]. The high Co³⁺/Co²⁺ in the Se-FeO_x-Co-2 sample demonstrates that the Co valence in Se-FeO_x-Co-2 mainly exists as Co³⁺. In conclusion, the incorporated Co effectively transformed more electrons into Fe, which was beneficial for increasing catalytic performance.

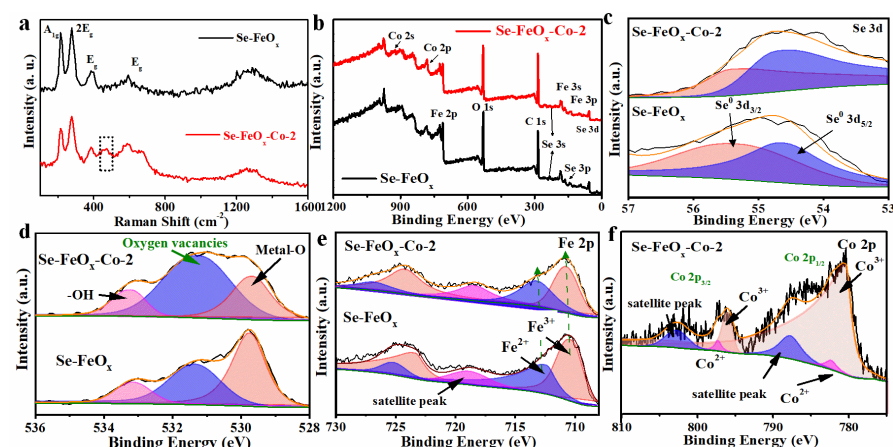


Figure 2. (a) Raman spectra of Se-FeO_x and Se-FeO_x-Co-2 samples. (b) XPS full survey spectra of those powders. High-resolution XPS spectra of (c) Se 3d, (d) O 1s, (e) Fe 2p, and (f) Co 2p for Se-FeO_x and Se-FeO_x-Co-2 samples.

After characterizing the structural properties of the different catalysts, the electrocatalytic performances were evaluated in the KOH solution. The ORR and OER performances of those Se-FeO_x-based catalysts were measured using LSV curves in a three-electrode system. Regarding the CV test of the Se-FeO_x and Se-FeO_x-Co-2 samples, Figure 3a displays distinct cathodic ORR peaks within the same voltage window at room temperature in 0.1 M KOH solution with an O₂-saturated environment. The clear oxygen reduction peaks of Se-FeO_x and Se-FeO_x-Co-2 under an O₂ atmosphere suggest their catalytic activity for oxygen conversion [59]. A peak at 0.64 V versus RHE is observed, which is higher than the Se-FeO_x peak at 0.52 V in Se-FeO_x. This demonstrates the prominent ORR activity for Se-FeO_x-Co-2 [60]. In addition, the ORR peak current of Se-FeO_x-Co-2 reaches 0.12 mA cm⁻², which is better than that of Se-FeO_x (with a peak current of 0.06 mA cm⁻²) [61]. As shown in Figure 3b, the ORR performance of the samples was compared at 1600 rpm. Se-FeO_x-Co-2 had a high onset potential ($E_{\text{onset}} = 0.76$ V) and high half-wave potential ($E_{1/2} = 0.64$ V). However, the onset potential of Se-FeO_x was 0.66 V, and the half-wave potential was 0.52 V. In addition, the onset potential of Se-FeO_x-Co-1 was 0.70 V, with

a half-wave potential of 0.59 V. Therefore, the Se-FeO_x-Co-2 showed the best ORR performance. Further, Se-FeO_x-Co-2 also exhibited excellent OER characteristics among the three catalysts. As shown in Figure 3c, it required an overpotential of only 280 mV to reach a current density of 10 mA·cm⁻² for the Se-FeO_x-Co-2. By contrast, Se-FeO_x and Se-FeO_x-Co-1 showed larger overpotentials of 400 and 290 mV to reach 10 mA·cm⁻², respectively. The relative performance comparison of all catalysts is summarized in Figures 3d and S4. It can be seen that the potential gaps of Se-FeO_x, Se-FeO_x-Co-1, and Se-FeO_x-Co-2 are 1.11, 0.93, and 0.87 V, which implied that the as-prepared Se-FeO_x-Co-2 showed significantly enhanced catalytic activity towards ORR and OER. Moreover, the lowered potential gap contributes to the charging/discharging performance of the ZAB devices. Compared with some reported references, the Se-FeO_x-Co-2 material shows excellent performance in the same alkaline environment (Table S1) [62–68]. In addition, the stability of ORR and OER were analyzed using chronoamperometry. As shown in Figure 3e,f, after a 14 h measurement of the ORR process, 91.5% of the initial current density was maintained in Se-FeO_x-Co-2, which was superior to Se-FeO_x (only 59.2% after 10 h). In addition, Se-FeO_x-Co-2 still showed long-term stability for 20 h in the OER process, which was much longer than that of Se-FeO_x in the same conditions. Therefore, the Se-FeO_x-Co-2 outperformed the other samples in both activity and stability. The enhanced electrocatalytic performance of Se-FeO_x-Co-2 might be owing to the following reasons: First, the loosely stacked nanoflakes of Se-FeO_x-Co-2 help to improve the electrochemical surface area, and therefore, more active sites are exposed [69,70]. Second, the Co dopants significantly enhance the conductivity of the FeO_x and, thus, facilitate the charge and electron transfer during the electrochemical reaction, which contributes to improving the activity [71,72]. Third, as evidenced by the XPS results, an electronic interaction occurs after introducing Co into FeO_x, and therefore, the synergistic effect between different metals significantly improves the electrocatalytic performance.

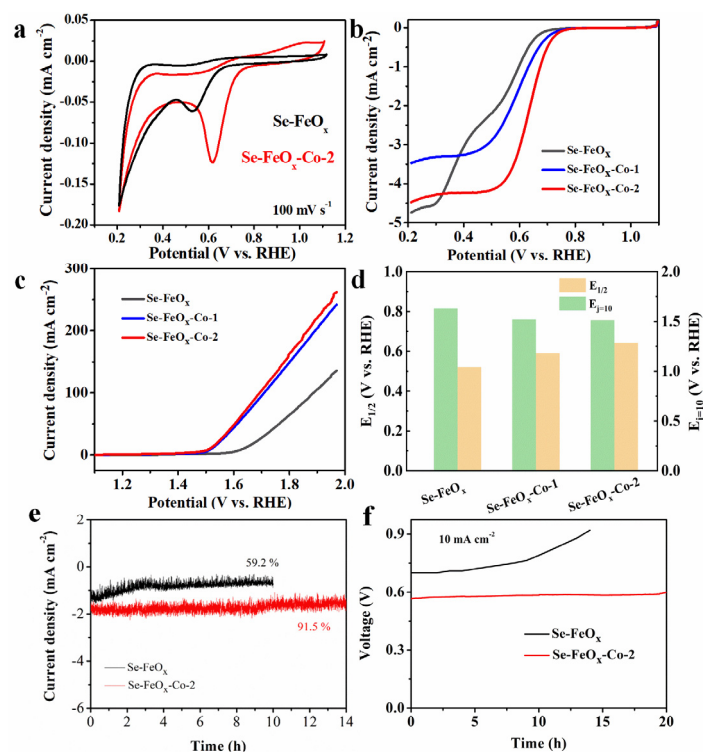


Figure 3. (a) CV curves of Se-FeO_x-Co and Se-FeO_x-Co-2 catalyst at 100 mV s⁻¹. (b) LSV curves of a series of Se-FeO_x sample catalysts at 1600 rpm for ORR test. (c) LSV curves of catalysts for OER test. (d) Relative bar in the value of $E_{1/2}$ and $E_{j=10}$ in a series of samples. (e) ORR stability of catalysts tested in half-wave potential, and (f) OER stability of catalysts at a current density of 10 mA cm⁻².

To further evaluate the practical properties of the Se-FeO_x-Co-2 catalyst in energy conversion and storage devices, a rechargeable ZAB was assembled. A schematic of the operation of the ZABs is shown in Figure 4a. A ZAB assembled with the Se-FeO_x catalyst was used as the control sample under the same conditions. As shown in Figure 4b,c, the ZAB with the Se-FeO_x-Co-2 catalyst exhibited a stable open-circuit voltage far higher than that of Se-FeO_x (1.16 V). As shown in Figure 4d, the Se-FeO_x-Co-2-based ZAB delivered a dischargeable capacity of 391 mAh g⁻¹, significantly larger than that of the Se-FeO_x based ZAB (215 mAh g⁻¹). This improved performance is related to the optimized oxygen catalysis properties of the Se-FeO_x-Co-2 catalyst. Moreover, the battery, which consists of a Se-FeO_x-Co-2 catalyst, exhibits a higher power density of 68 mW cm⁻² than that of the Se-FeO_x-based battery (only 54 mW cm⁻²) in Figure S5. The long-term cycling stability of the rechargeable ZAB with Se-FeO_x-Co-2 and Se-FeO_x was measured, as shown in Figure 4e. A slight voltage change was observed over 800 min during discharge/charge cycling, consistent with the good electrocatalytic stability of Se-FeO_x-Co-2. The Se-FeO_x-based ZAB showed poor cycling performance and could not operate normally after 570 min (with a low discharging platform of 0.5 V). The above results also confirmed that Se-FeO_x-Co-2, with high activity and stability, has significant potential for application as an electrode catalyst in ZABs.

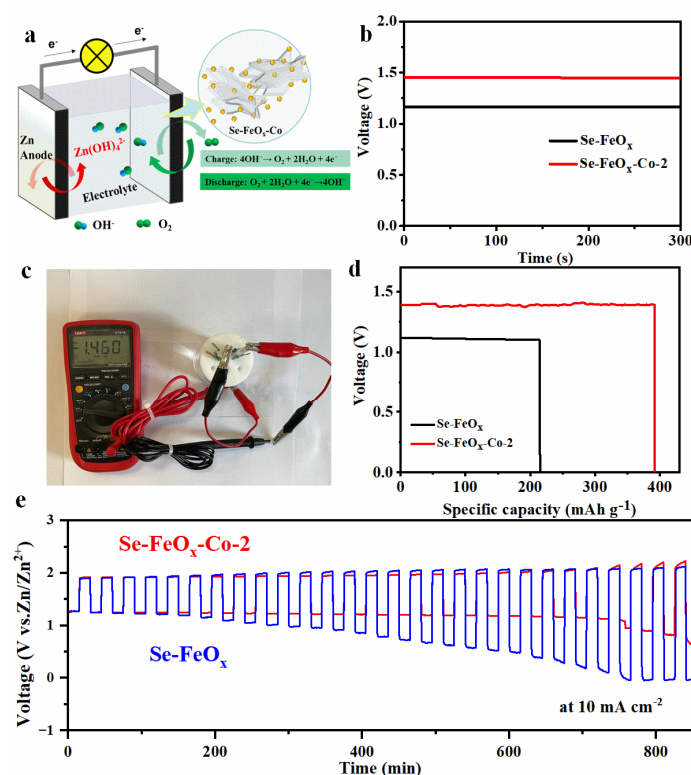


Figure 4. (a) Schematic of the operation of zinc-air battery (ZAB) based on the Se-FeO_x-Co bifunctional catalyst. (b) Comparison of open-circuit voltage and (c) optical photograph of ZAB based on Se-FeO_x-Co-2. (d) Discharging curves and (e) rechargeable ZAB cycling profiles at current density of 10 mA cm⁻².

4. Conclusions

In conclusion, Se QD@ CoFeO_x composite materials were synthesized using a hydrothermal process. During the synthesis process, the SeO₂ precursor used as the Se source decomposed to form Se QDs and iron oxide was generated simultaneously. At high temperatures and pressures, numerous Co²⁺ ions were doped into the crystal lattice of iron oxide. The nanostructure and valence state of the materials were investigated via SEM, TEM, HRTEM, XRD, Raman spectroscopy, and X-ray photoelectron spectroscopy (XPS). All successfully demonstrated the insertion of cobalt ions into the iron oxide lattice, which

had a positive effect on the exposure of active sites, fast charge and electron transfer, and electron interactions in the electrochemical process. Because the Co ions were successfully incorporated into the iron oxide lattice, the as-prepared catalyst showed high activity for oxygen catalysis, with a potential gap of only 0.87 V. In addition, it displayed a satisfactory open-circuit voltage (1.46 V) and long-term durability of over 800 min when fabricated into a liquid ZAB. Therefore, the Se QD@CoFeO_x catalyst is one of the most promising candidates for practical applications. Our research explores new prospects for the development of cathodic materials for ZABs.

Supplementary Materials: The following supporting information can be downloaded at: <https://www.mdpi.com/article/10.3390/batteries9110561/s1>, Figure S1: SEM and TEM images of Se-FeO_x material; Figure S2: SEM and TEM images of Se-FeO_x-Co-1 material; Figure S3: The Co 2p spectra of Se-FeO_x-Co-1 and Se-FeO_x-Co-2 materials. Figure S4: The relative bar in the value of E_{j=10}-E_{1/2}; Figure S5: The polarization and power density curves of Se-FeO_x and Se-FeO_x-Co-2 materials as cathode. Table S1. The ORR and OER performance comparison with reported references.

Author Contributions: Conceptualization, D.Z., Y.W., X.H. and W.H.; methodology, D.Z. and X.H.; investigation, X.H. and W.H.; resources, X.H. and W.H.; writing—original draft preparation, D.Z.; writing—review and editing, X.H.; supervision, X.H. and W.H.; project administration, X.H. and W.H.; funding acquisition, X.H. and W.H. All authors have read and agreed to the published version of the manuscript.

Funding: This research was funded by the National Natural Science Foundation of China, grant number U22A20119.

Data Availability Statement: The data presented in this study are contained within the article.

Conflicts of Interest: The authors declare no conflict of interest.

References

- Zhang, S.; Li, S.; Lu, Y. Designing safer lithium-based batteries with nonflammable electrolytes: A review. *eScience* **2021**, *1*, 163–177. [[CrossRef](#)]
- Yuan, M.; Sun, Z.; Yang, H.; Wang, D.; Liu, Q.; Nan, C.; Li, H.; Sun, G.; Chen, S. Self-catalyzed rechargeable lithium-air battery by *in situ* metal ion doping of discharge products: A combined theoretical and experimental study. *Energy Environ. Mater.* **2023**, *6*, e12258. [[CrossRef](#)]
- Cheng, F.; Chen, J. Metal–air batteries: From oxygen reduction electrochemistry to cathode catalysts. *Chem. Soc. Rev.* **2012**, *41*, 2172–2192. [[CrossRef](#)]
- Niu, Y.; Gong, S.; Liu, X.; Xu, C.; Xu, M.; Sun, S.-G.; Chen, Z. Engineering iron-group bimetallic nanotubes as efficient bifunctional oxygen electrocatalysts for flexible Zn–air batteries. *eScience* **2022**, *2*, 546–556. [[CrossRef](#)]
- Yu, H.; Fan, F.; He, C.; Zhou, M.; Ma, T.; Wang, Y.; Cheng, C. Sulfur-modulated FeNi nanoalloys as bifunctional oxygen electrode for efficient rechargeable aqueous Zn–air batteries. *Sci. China Mater.* **2022**, *65*, 3007–3016. [[CrossRef](#)]
- Xin, L.; Yang, F.; Rasouli, S.; Qiu, Y.; Li, Z.-F.; Uzunoglu, A.; Sun, C.-J.; Liu, Y.; Ferreira, P.; Li, W.; et al. Understanding Pt nanoparticle anchoring on graphene supports through surface functionalization. *ACS Catal.* **2016**, *6*, 2642–2653. [[CrossRef](#)]
- Liu, H.; Liu, Q.; Wang, Y.; Wang, Y.; Chou, S.; Hu, Z.; Zhang, Z. Bifunctional carbon-based cathode catalysts for zinc–air battery: A review. *Chin. Chem. Lett.* **2022**, *33*, 683–692. [[CrossRef](#)]
- Zhang, W.; Lai, W.; Cao, R. Energy-related small molecule activation reactions: Oxygen reduction and hydrogen and oxygen evolution reactions catalyzed by porphyrin- and corrole-based systems. *Chem. Rev.* **2017**, *117*, 3717–3797. [[CrossRef](#)]
- Wang, X.; Li, Z.; Qu, Y.; Yuan, T.; Wang, W.; Wu, Y.; Li, Y. Review of metal catalysts for oxygen reduction reaction: From nanoscale engineering to atomic design. *Chem.* **2019**, *5*, 1486–1511. [[CrossRef](#)]
- Peng, X.; Zhang, L.; Chen, Z.; Zhong, L.; Zhao, D.; Chi, X.; Zhao, X.; Li, L.; Lu, X.; Leng, K.; et al. Hierarchically porous carbon plates derived from wood as bifunctional ORR/OER electrodes. *Adv. Mater.* **2019**, *31*, 1900341. [[CrossRef](#)]
- Yu, J.; Li, Z.; Liu, T.; Zhao, S.; Guan, D.; Chen, D.; Shao, Z.; Ni, M. Morphology control and electronic tailoring of CoxAy (A = P, S, Se) electrocatalysts for water splitting. *Chem. Eng. J.* **2023**, *460*, 141674. [[CrossRef](#)]
- Liu, B.; Wang, X.; Wang, R.; Zhang, G.; Xu, X.; Liu, J.; Sun, Z.; Liu, M.; Wang, C.; Meng, X.; et al. Activating and stabilizing Co sites in CoP for triggering oxygen electrocatalysis in zinc–air battery. *Chem. Eng. J.* **2023**, *475*, 146154. [[CrossRef](#)]
- Qi, P.; Chen, M.; Luo, T.; Zhao, C.; Lin, C.; Luo, H.; Zhang, D. Solid-state self-catalyzed growth of N-doped carbon tentacles on an M(Fe, Co)Se surface for rechargeable Zn–air batteries. *Chem. Commun.* **2023**, *59*, 5898–5901. [[CrossRef](#)]
- Gui, F.; Jin, Q.; Xiao, D.; Jin, Z.; Zhang, Y.; Cao, Y.; Yang, M.; Tan, Q.; Zhang, C.; Siahrostami, S.; et al. High-performance zinc–air batteries enabled by hybridizing atomically dispersed FeN₂ with Co₃O₄ nanoparticles. *J. Mater. Chem. A* **2023**, *11*, 1312–1323. [[CrossRef](#)]

15. Wu, L.; Li, J.; Shi, C.; Li, Y.; Mi, H.; Deng, L.; Zhang, Q.; He, C.; Ren, X. Rational design of the FeS₂/NiS₂ heterojunction interface structure to enhance the oxygen electrocatalytic performance for zinc–air batteries. *J. Mater. Chem. A* **2022**, *10*, 16627–16638. [[CrossRef](#)]
16. Wang, J.-J.; Li, X.-P.; Cui, B.-F.; Zhang, Z.; Hu, X.-F.; Ding, J.; Deng, Y.-D.; Han, X.-P.; Hu, W.-B. A review of non-noble metal-based electrocatalysts for CO₂ electroreduction. *Rare Met.* **2021**, *40*, 3019–3037. [[CrossRef](#)]
17. Wang, Y.; Wu, X.; Jiang, X.; Wu, X.; Tang, Y.; Sun, D.; Fu, G. Citrulline-induced mesoporous CoS/CoO heterojunction nanorods triggering high-efficiency oxygen electrocatalysis in solid-state Zn-air batteries. *Chem. Eng. J.* **2022**, *434*, 134744. [[CrossRef](#)]
18. Weng, C.; Lv, X.; Ren, J.; Wang, Y.; Tian, W.; Gao, L.; Wang, H.; Yuan, Z. Self-promoted electrocatalysts derived from surface reconstruction for rechargeable Zinc–air batteries. *ACS Sustain. Chem. Eng.* **2022**, *10*, 6456–6465. [[CrossRef](#)]
19. Zhang, Z.; Liang, X.; Li, J.; Qian, J.; Liu, Y.; Yang, S.; Wang, Y.; Gao, D.; Xue, D. Interfacial engineering of NiO/NiCo₂O₄ porous nanofibers as efficient bifunctional catalysts for rechargeable Zinc–air batteries. *ACS Appl. Mater. Interfaces* **2020**, *12*, 21661–21669. [[CrossRef](#)]
20. Agyeman, D.; Zheng, Y.; Lee, T.; Park, M.; Tamakloe, W.; Lee, G.; Jang, H.; Cho, K.; Kang, Y. Synergistic catalysis of the lattice oxygen and transition metal facilitating ORR and OER in perovskite catalysts for Li–O₂ batteries. *ACS Catal.* **2021**, *11*, 424–434. [[CrossRef](#)]
21. Huang, H.; Huang, A.; Liu, D.; Han, W.; Kuo, C.; Chen, H.; Li, L.; Pan, H.; Peng, S. Tailoring oxygen reduction reaction kinetics on perovskite oxides via oxygen vacancies for low-temperature and knittable zinc–air batteries. *Adv. Mater.* **2023**, *35*, 2303109. [[CrossRef](#)] [[PubMed](#)]
22. Kumar, R.S.; Prabhakaran, S.; Ramakrishnan, S.; Karthikeyan, S.C.; Kim, A.R.; Kim, D.H.; Yoo, D.J. Developing outstanding bifunctional electrocatalysts for rechargeable Zn-air batteries using high-purity spinel-type ZnCo₂Se₄ nanoparticles. *Small* **2023**, *19*, 2207096. [[CrossRef](#)] [[PubMed](#)]
23. Guan, D.; Shi, C.; Xu, H.; Gu, Y.; Zhong, J.; Sha, Y.; Hu, Z.; Ni, M.; Shao, Z. Simultaneously mastering operando strain and reconstruction effects via phase-segregation strategy for enhanced oxygen-evolving electrocatalysis. *J. Energy Chem.* **2023**, *82*, 572–580. [[CrossRef](#)]
24. Li, H.; Askari, S.; Wang, J.; Wolff, N.; Behrens, M.; Kienle, L.; Benedikt, J. Nitrogen-doped NiCo₂O₄ nanowires on carbon paper as a self-supported air cathode for rechargeable Zn-air batteries. *Int. J. Hydrog. Energy* **2023**, *48*, 26107–26118. [[CrossRef](#)]
25. Bo, L.; Nian, F.; Pu, L.; Li, P.; Hu, Y.; Tong, J. Simply embedding α-Fe₂O₃/Fe₃O₄ nanoparticles in N-doped graphitic carbon polyhedron layered arrays as excellent electrocatalyst for rechargeable Zn-air battery. *Sep. Purif. Technol.* **2023**, *312*, 123413. [[CrossRef](#)]
26. Samanta, A.; Das, S.; Jana, S. Doping of Ni in α-Fe₂O₃ nanoclews to boost oxygen evolution electrocatalysis. *ACS Sustain. Chem. Eng.* **2019**, *7*, 12117–12124. [[CrossRef](#)]
27. Niu, Y.; Yuan, Y.; Zhang, Q.; Chang, F.; Yang, L.; Chen, Z.; Bai, Z. Morphology-controlled synthesis of metal-organic frameworks derived lattice plane-altered iron oxide for efficient trifunctional electrocatalysts. *Nano Energy* **2021**, *82*, 105699. [[CrossRef](#)]
28. Zhu, S.; Tian, H.; Wang, N.; Chen, B.; Mai, Y.; Feng, X. Patterning graphene surfaces with iron-oxide-embedded mesoporous polypyrrole and derived N-doped carbon of tunable pore size. *Small* **2018**, *14*, 1702755. [[CrossRef](#)]
29. Hof, F.; Liu, M.; Valenti, G.; Picheau, E.; Paolucci, F.; Pénicaud, A. Size control of nanographene supported iron oxide nanoparticles enhances their electrocatalytic performance for the oxygen reduction and oxygen evolution reactions. *J. Phys. Chem. C* **2019**, *123*, 20774–20780. [[CrossRef](#)]
30. Chen, M.; Huang, Z.; Ye, X.; Zhang, L.; Feng, J.; Wang, A. Caffeine derived graphene-wrapped Fe₃C nanoparticles entrapped in hierarchically porous FeNC nanosheets for boosting oxygen reduction reaction. *J. Colloid Interface Sci.* **2023**, *637*, 216–224. [[CrossRef](#)]
31. Wang, M.; Ji, S.; Wang, H.; Wang, X.; Linkov, V.; Wang, R. Foamed carbon-supported nickel-iron oxides interspersed with bamboo-like carbon nanotubes for high-performance rechargeable Zinc–air batteries. *Small* **2022**, *18*, 2204474. [[CrossRef](#)] [[PubMed](#)]
32. Fan, Z.; Li, J.; Yang, W.; Fu, Q.; Sun, K.; Song, Y.; Wei, Z.; Liao, Q.; Zhu, X. Green and facile synthesis of iron oxide nanoparticle-embedded N-doped biocarbon as an efficient oxygen reduction electrocatalyst for microbial fuel cells. *Chem. Eng. J.* **2020**, *385*, 123393. [[CrossRef](#)]
33. Xiao, Z.; Wu, C.; Wang, W.; Pan, L.; Zou, J.; Wang, L.; Zhang, X.; Li, G. Tailoring the hetero-structure of iron oxides in the framework of nitrogen doped carbon for the oxygen reduction reaction and zinc–air batteries. *J. Mater. Chem. A* **2020**, *8*, 25791–25804. [[CrossRef](#)]
34. Rasal, A.S.; Yadav, S.; Yadav, A.; Kashale, A.A.; Manjunatha, S.T.; Altaee, A.; Chang, J.Y. Carbon quantum dots for energy applications: A review. *ACS Appl. Nano Mater.* **2021**, *4*, 6515–6541. [[CrossRef](#)]
35. García de Arquer, F.P.; Talapin, D.V.; Klimov, V.I.; Arakawa, Y.; Bayer, M.; Sargent, E.H. Semiconductor quantum dots: Technological progress and future challenges. *Science* **2021**, *373*, eaaz8541. [[CrossRef](#)]
36. Meng, D.; Wei, L.; Shi, J.; Jiang, Q.; Tang, J. A review of enhanced electrocatalytic composites hydrogen/oxygen evolution based on quantum dot. *J. Ind. Eng. Chem.* **2023**, *121*, 27–39. [[CrossRef](#)]
37. Yu, Y.; Ma, T.; Huang, H. Semiconducting quantum dots for energy conversion and storage. *Adv. Funct. Mater.* **2023**, *33*, 2213770. [[CrossRef](#)]

38. Qian, J.; Guo, X.; Wang, T.; Liu, P.; Zhang, H.; Gao, D. Bifunctional porous Co-doped NiO nanoflowers electrocatalysts for rechargeable zinc-air batteries. *Appl. Catal. B Environ.* **2019**, *250*, 71–77. [[CrossRef](#)]
39. Lian, Y.; Yang, W.; Zhang, C.; Sun, H.; Deng, Z.; Xu, W.; Song, L.; Ouyang, Z.; Wang, Z.; Guo, J.; et al. Unpaired 3d electrons on atomically dispersed cobalt centres in coordination polymers regulate both oxygen reduction reaction (ORR) activity and selectivity for use in zinc–air batteries. *Angew. Chem. Int. Ed.* **2020**, *59*, 286–294. [[CrossRef](#)]
40. Ramakrishnan, S.; Velusamy, D.B.; Sengodan, S.; Nagaraju, G.; Kim, D.H.; Kim, A.R.; Yoo, D.J. Rational design of multifunctional electrocatalyst: An approach towards efficient overall water splitting and rechargeable flexible solid-state zinc–air battery. *Appl. Catal. B Environ.* **2022**, *300*, 120752. [[CrossRef](#)]
41. Li, Y.-S.; Church, J.S.; Woodhead, A.L. Infrared and Raman spectroscopic studies on iron oxide magnetic nano-particles and their surface modifications. *J. Magn. Magn. Mater.* **2012**, *324*, 1543–1550. [[CrossRef](#)]
42. El Mendili, Y.; Bardeau, J.F.; Randrianantoandro, N.; Gourbil, A.; Grenache, J.M.; Mercier, A.M.; Grasset, F. New evidences of in situ laser irradiation effects on γ -Fe₂O₃ nanoparticles: A Raman spectroscopic study. *J. Raman Spectrosc.* **2011**, *42*, 239–242. [[CrossRef](#)]
43. Zheng, H.; Bao, J.; Huang, Y.; Xiang, L.; Faheem; Ren, B.; Du, J.; Nadagouda, M.N.; Dionysiou, D.D. Efficient degradation of atrazine with porous sulfurized Fe₂O₃ as catalyst for peroxyomonosulfate activation. *Appl. Catal. B Environ.* **2019**, *259*, 118056. [[CrossRef](#)]
44. Karuppasamy, P.; Karthika, A.; Senthilkumar, S.; Rajapandian, V. An efficient and highly sensitive amperometric quercetin sensor based on a lotus flower like SeO₂-decorated rGO nanocomposite modified glassy carbon electrode. *Electrocatalysis* **2022**, *13*, 269–282. [[CrossRef](#)]
45. Wu, Z.; Lin, X.; Zhang, J.; Chu, X.; Xu, J.; Li, J.; Liu, Y.; Yu, H.; Yan, L.; Zhang, L.; et al. Encapsulating selenium into mesoporous carbon for high-performance aqueous Cu-Se battery. *Chem. Eng. J.* **2023**, *454*, 140433. [[CrossRef](#)]
46. Liu, K.; Niu, J.; Liu, L.; Tian, F.; Nie, H.; Liu, X.; Chen, K.; Zhao, R.; Sun, S.; Jiao, M.; et al. LUMO-mediated Se and HOMO-mediated Te nanozymes for selective redox biocatalysis. *Nano Lett.* **2023**, *23*, 5131–5140. [[CrossRef](#)]
47. Sapna; Budhiraja, N.; Kumar, V.; Singh, S.K. Synergistic effect in structural and supercapacitor performance of well dispersed CoFe₂O₄/Co₃O₄ nano-hetrostructures. *Ceram. Int.* **2018**, *44*, 13806–13814. [[CrossRef](#)]
48. Chen, H.; Liu, W.; Qin, Z. ZnO/ZnFe₂O₄ nanocomposite as a broad-spectrum photo-Fenton-like photocatalyst with near-infrared activity. *Catal. Sci. Technol.* **2017**, *7*, 2236–2244. [[CrossRef](#)]
49. Li, C.; Lin, Y.; Li, X.; Li, Z.; Luo, P.; Jin, Y.; Li, Z. Effect of Co-doping concentration on α -Fe₂O₃/Graphene as anode materials for lithium ion batteries. *Colloids Surf. A Physicochem. Eng. Asp.* **2023**, *660*, 130681. [[CrossRef](#)]
50. Liu, G.; Li, J.; Fu, J.; Jiang, G.; Lui, G.; Luo, D.; Deng, Y.P.; Zhang, J.; Cano, Z.P.; Yu, A.; et al. An oxygen-vacancy-rich semiconductor-supported bifunctional catalyst for efficient and stable zinc–air batteries. *Adv. Mater.* **2019**, *31*, 1806761. [[CrossRef](#)]
51. Qin, J.; Liu, Z.; Wu, D.; Yang, J. Optimizing the electronic structure of cobalt via synergized oxygen vacancy and Co-N-C to boost reversible oxygen electrocatalysis for rechargeable Zn-air batteries. *Appl. Catal. B Environ.* **2020**, *278*, 119300. [[CrossRef](#)]
52. Han, X.; Liu, C.; Tang, Y.; Meng, Q.; Zhou, W.; Chen, S.; Deng, S.; Wang, J. Unveiling the role of cobalt doping in optimizing ammonia electrosynthesis on iron–cobalt oxyhydroxide hollow nanocages. *J. Mater. Chem. A* **2023**, *11*, 14424–14431. [[CrossRef](#)]
53. Li, M.; Tang, Y.; Shi, W.; Chen, F.; Shi, Y.; Gu, H. Design of visible-light-response core–shell Fe₂O₃/CuBi₂O₄ heterojunctions with enhanced photocatalytic activity towards the degradation of tetracycline: Z-scheme photocatalytic mechanism insight. *Inorg. Chem. Front.* **2018**, *5*, 3148–3154. [[CrossRef](#)]
54. Zhu, H.; Dong, S.; Du, X.; Du, H.; Xia, J.; Liu, Q.; Luo, Y.; Guo, H.; Li, T. Defective CuO-rich CuFe₂O₄ nanofibers enable the efficient synergistic electrochemical reduction of nitrate to ammonia. *Catal. Sci. Technol.* **2022**, *12*, 4998–5002. [[CrossRef](#)]
55. Luo, J.; Han, X.; Ge, J.; Wang, Y.; Zhao, X.; Zhang, F.; Lei, X. Cu₉S₅/Fe₂O₃ nanospheres as advanced negative electrode materials for high performance battery-like hybrid capacitors. *ACS Appl. Energy Mater.* **2022**, *5*, 7016–7025. [[CrossRef](#)]
56. Yang, H.; Wang, B.; Li, H.; Ni, B.; Wang, K.; Zhang, Q.; Wang, X. Trimetallic sulfide mesoporous nanospheres as superior electrocatalysts for rechargeable Zn–air batteries. *Adv. Energy Mater.* **2018**, *8*, 1801839. [[CrossRef](#)]
57. Guo, Y.; Wang, T.; Yang, Q.; Li, X.; Li, H.; Wang, Y.; Jiao, T.; Huang, Z.; Dong, B.; Zhang, W.; et al. Highly efficient electrochemical reduction of nitrogen to ammonia on surface termination modified Ti₃C₂T_x MXene nanosheets. *ACS Nano* **2020**, *14*, 9089–9097. [[CrossRef](#)]
58. Zhang, G.; Wang, S.; Zeng, X.; Li, X.; Xiao, L.; Chen, K.; Lu, Q.; Xu, Q.; Weng, J.; Xu, J. Holey amorphous FeCoO-coated black phosphorus for robust polysulfide adsorption and catalytic conversion in lithium–sulfur batteries. *J. Mater. Chem. A* **2022**, *10*, 11676–11683. [[CrossRef](#)]
59. Lee, K.; Zhang, L.; Lui, H.; Hui, R.; Shi, Z.; Zhang, J. Oxygen reduction reaction (ORR) catalyzed by carbon-supported cobalt polypyrrole (Co-PPy/C) electrocatalysts. *Electrochim. Acta* **2009**, *54*, 4704–4711. [[CrossRef](#)]
60. Xu, C.; Guo, C.; Liu, J.; Hu, B.; Dai, J.; Wang, M.; Jin, R.; Luo, Z.; Li, H.; Chen, C. Accelerating the oxygen adsorption kinetics to regulate the oxygen reduction catalysis via Fe3C nanoparticles coupled with single Fe-N₄ sites. *Energy Storage Mater.* **2022**, *51*, 149–158. [[CrossRef](#)]
61. Gao, S.; Fan, B.; Feng, R.; Ye, C.; Wei, X.; Liu, J.; Bu, X. N-doped-carbon-coated Fe₃O₄ from metal-organic framework as efficient electrocatalyst for ORR. *Nano Energy* **2017**, *40*, 462–470. [[CrossRef](#)]
62. Mao, S.; Wen, Z.; Huang, T.; Hou, Y.; Chen, J. High-performance bi-functional electrocatalysts of 3D crumpled graphene–cobalt oxide nanohybrids for oxygen reduction and evolution reactions. *Energy Environ. Sci.* **2014**, *7*, 609–616. [[CrossRef](#)]

63. Du, S.; Ren, Z.; Qu, Y.; Wu, J.; Xi, W.; Zhu, J.; Fu, H. Co_3O_4 nanosheets as a high-performance catalyst for oxygen evolution proceeding via a double two-electron process. *Chem. Commun.* **2016**, *52*, 6705–6708. [[CrossRef](#)]
64. Tian, G.; Zhao, M.; Yu, D.; Kong, X.; Huang, J.; Zhang, Q.; Wei, F. Nitrogen-doped graphene/carbon nanotube hybrids: In situ formation on bifunctional catalysts and their superior electrocatalytic activity for oxygen evolution/reduction reaction. *Small* **2014**, *10*, 2251–2259. [[CrossRef](#)] [[PubMed](#)]
65. Rasaki, S.A.; Chen, Z.; Shen, H.; Guo, H.; Thomas, T.; Yang, M. Cobalt nanoparticles modified single-walled titanium carbonitride nanotube derived from solid-solid separation for oxygen reduction reaction in alkaline solution. *Electrocatalysis* **2020**, *11*, 579–592. [[CrossRef](#)]
66. Tang, K.; Hu, H.; Xiong, Y.; Chen, L.; Zhang, J.; Yuan, C.; Wu, M. Hydrophobization engineering of the air–cathode catalyst for improved oxygen diffusion towards efficient zinc–air batteries. *Angew. Chem. Int. Ed.* **2022**, *61*, e202202671. [[CrossRef](#)]
67. Faisal, S.N.; Haque, E.; Noorbehesht, N.; Liu, H.; Islam, M.M.; Shabnam, L.; Roy, A.K.; Pourazadi, E.; Islam, M.S.; Harris, A.T.; et al. A quadrafunctional electrocatalyst of nickel/nickel oxide embedded N-graphene for oxygen reduction, oxygen evolution, hydrogen evolution and hydrogen peroxide oxidation reactions. *Sustain. Energy Fuels* **2018**, *2*, 2081–2089. [[CrossRef](#)]
68. Shudo, Y.; Fukuda, M.; Islam, M.S.; Kuroiwa, K.; Sekine, Y.; Karim, M.R.; Hayami, S. 3D porous Ni/ NiO_x as a bifunctional oxygen electrocatalyst derived from freeze-dried $\text{Ni}(\text{OH})_2$. *Nanoscale* **2021**, *13*, 5530–5535. [[CrossRef](#)]
69. Xiong, P.; Sun, B.; Sakai, N.; Ma, R.; Sasaki, T.; Wang, S.; Zhang, J.; Wang, G. 2D superlattices for efficient energy storage and conversion. *Adv. Mater.* **2020**, *32*, 1902654. [[CrossRef](#)]
70. Cheng, Y.; Pang, K.; Wu, X.; Zhang, Z.; Xu, X.; Ren, J.; Huang, W.; Song, R. In situ hydrothermal synthesis MoS_2 /guar gum carbon nanoflowers as advanced electrocatalysts for electrocatalytic hydrogen evolution. *ACS Sustain. Chem. Eng.* **2018**, *6*, 8688–8696. [[CrossRef](#)]
71. Kong, H.; Lv, C.; Yan, C.; Chen, G. Engineering mesoporous single crystals Co-doped Fe_2O_3 for high-performance lithium ion batteries. *Inorg. Chem.* **2017**, *56*, 7642–7649. [[CrossRef](#)] [[PubMed](#)]
72. Hou, Y.; Zuo, F.; Dagg, A.; Feng, P. A three-dimensional branched cobalt-doped $\alpha\text{-Fe}_2\text{O}_3$ Nanorod/ MgFe_2O_4 heterojunction array as a flexible photoanode for efficient photoelectrochemical water oxidation. *Angew. Chem. Int. Ed.* **2013**, *52*, 1248–1252. [[CrossRef](#)] [[PubMed](#)]

Disclaimer/Publisher’s Note: The statements, opinions and data contained in all publications are solely those of the individual author(s) and contributor(s) and not of MDPI and/or the editor(s). MDPI and/or the editor(s) disclaim responsibility for any injury to people or property resulting from any ideas, methods, instructions or products referred to in the content.